Hindawi
IET Signal Processing
Volume 2024, Article ID 5026821, 12 pages
https://doi.org/10.1049/2024/5026821

Research Article

Deep Anomaly Detection with Attention (DADA): A Novel Approach for Identifying Multipath Interference in Radar Signals

Kang Yan[1], **Weidong Jin**[1], **Yingkun Huang**[2], **Zhenhua Li**[3], **Pucha Song**[4] and **Ligang Huang**[5]

[1]*School of Electrical Engineering, Southwest Jiaotong University, Chengdu, China*
[2]*National Supercomputing Center in Shenzhen, Shenzhen, China*
[3]*Department of Electronic Engineering, College of Electronic and Information Engineering, Guangdong Ocean University, Zhanjiang, China*
[4]*School of Electronic Information and Electrical Engineering, Chengdu University, Chengdu, China*
[5]*Beijing Institute of Remote Sensing Equipment, Beijing, China*

Correspondence should be addressed to Kang Yan; kangyan@my.swjtu.edu.cn

Received 25 May 2023; Revised 5 December 2023; Accepted 31 December 2023; Published 13 January 2024

Academic Editor: Hasan Mir

Multipath interference in radar signals caused by sea, ground, and other environments poses significant challenges to the target detection, tracking, and classification capabilities of radar systems. Existing methods for radar signal identification require labeled samples and focus mainly on the classification of normal signals. However, in practice, anomalous samples (multipath interference signals) may be scarce and highly imbalanced (i.e., mostly normal samples). To address this problem, we propose a deep anomaly detection with attention (DADA) for semisupervised detection of multipath radar signals. The method transforms radar signals into time–frequency images and is trained exclusively on normal samples. The autoencoder architecture is extended with a feature extractor network to capture latent sample features. CBAM attention is introduced to improve feature extraction. By learning the distribution of normal samples in high-dimensional image space and low-dimensional feature space, a two-dimensional feature space representing normal samples is constructed. A one-class SVM then learns the boundary of normal samples for anomaly detection. Extensive experiments on radar signal datasets validate the effectiveness of the proposed approach.

1. Introduction

Multipath interference is a common problem in radar systems due to the reflections and diffraction of radar signals from the ground, sea, and other environments. As a result, the transmitted signal travels along multiple paths before arriving at the receiver [1]. The superposition of these delayed versions of the original signal causes distortion, resulting in the interference that can degrade the radar's performance in detecting, tracking, and classifying targets. In particular, this interference can affect the radar's ability to distinguish the true target signal from noise and clutter. For example, in the operation of shipboard radar reconnaissance equipment, signals may encounter multiple reflections from the sea surface, nearby islands, and the ship's own surface structures. In such situations, the radar system receives signals not only from the direct transmission path, but also from the various reflected paths, creating a multifaceted interference field. From a technical point of view, this affects not only the accuracy of the radar's measurement of signal amplitude and pulse width, but also the directional estimation of the signal. In the real-world electromagnetic environment of the battlefield, the complex multipath effects can lead to a spike in false readings in the signal processing of the radar reconnaissance equipment. This can lead to tactical false alarms and missed targets. In extreme cases, it can even lead to a blockage of the radar's receive channels, critically affecting its tactical performance. Therefore, detection and identification of multipath induced spurious signals have become an essential task in the radar signal processing to mitigate these effects.

Traditional radar signal identification techniques typically extract features from signals in the time domain,

frequency domain, and time–frequency domain to identify different radar modulation signals. For example, the studies by Yibing et al. [2–4] mainly focus on a complexity feature extraction in the time domain, while the study by Lunden and Koivunen [5] uses power spectral density in the frequency domain for feature extraction. However, with the increasing complexity of the radar signals, methods based solely on the time or frequency domain often fail to achieve the desired identification results. As a result, time–frequency domain feature extraction has become a research hotspot in the field, as it can reveal more abundant properties of the radar signals. Several time–frequency transform methods, such as short-time Fourier transform (STFT) [6], fractional Fourier transform (FrFT) [7], Choi-Williams Distribution (CWD) [8], and smoothed pseudo Wigner–Ville distribution (SPWVD) [9, 10], have been widely used for radar signal feature extraction. The core idea of these methods is to convert radar signals into time–frequency images and use deep learning image processing techniques for signal identification. Although these methods are effective in classifying various normal radar signals that are received, they do not consider how to detect anomalous multipath signals. However, these methods provide a valuable insight that different types of radar signals demonstrate distinguishable differences in the time–frequency structure after time–frequency transformation. Specifically, if analysis shows that the time–frequency representations of multipath and normal signals have significant detectable differences, then such differences can be utilized to identify and detect multipath signals. In summary, time–frequency domain features have the potential to differentiate types of radar signals in complex electromagnetic environments, thus providing a viable new approach to the detection and identification of multipath signals.

Anomaly detection is a prominent research area, commonly confronted with the challenge of highly imbalanced data samples, where normal samples significantly outnumber the anomalous ones. In this scenario, traditional supervised deep learning classification models often underperform. Semisupervised anomaly detection methods have emerged as essential tools to address this problem. Schlegl et al. [11] employs the generator of the generative adversarial networks (GAN) learn the distribution of normal images. During testing, new images are inversely mapped to the latent space and the difference in latent space is assumed to reflect anomalies. This method requires iterative optimization to find the best matching representation in the latent space, resulting in low-computational efficiency. Zenati et al. [12] introduces an anomaly detection framework based on BiGAN, which learns the encoder simultaneously during the GAN training process. This achieves an end-to-end joint training procedure, eliminating the need for computationally expensive inverse latent space mapping during the testing phase. Akcay et al. [13, 14] adopt an anomaly detection strategy based on an adversarial training. This approach is trained using only normal samples and employs a reconstruction strategy to enable the network to learn the distribution of normal image samples in the latent space. However, the design of the model tends to lead to overfitting. Sabokrou et al. [15] also employs an adversarial training approach. This method reconstructs input data by learning latent space of normal data, and uses adversarial training to enhance model performance. When encountering anomalous data that differs significantly from the normal data, the reconstruction error of the model increases markedly, thereby achieving anomaly detection.

The core idea of these methods is that abnormal samples exhibit significant differences from normal samples in both the high-dimensional image space and the encoded low-dimensional latent space. Motivated by the results of such research, we develop a deep anomaly detection with attention (DADA) model for detecting multipath interference in radar signals. The method takes the time–frequency image of radar signals as input and trains the model using only normal radar signals. We extend the structure of autoencoders by incorporating a feature extractor to capture the latent feature space of normal samples. By simultaneously considering the high-dimensional image space and the encoded low-dimensional feature space, the feature distribution of normal samples can be more accurately captured. Then, by employing a one-class SVM to learn the boundary of the normal sample feature space, we can achieve efficient anomaly detection. In addition, to better capture the time–frequency characteristics of radar signals, especially the line portions representing the main structural features, we introduce the CBAM attention mechanism to enhance model performance. This mechanism allows the network to adaptively focus on the feature regions with the most structural differences in the signal. Therefore, the main innovations and contributions of this paper are summarized as follows:

(1) This paper proposes a semisupervised anomaly detection model for detecting multipath interference in the radar signals.
(2) Our model extends the typical autoencoder structure by incorporating a feature extractor to capture the latent feature space of time–frequency images. In addition, we employ the CBAM attention mechanism to focus on the key high-frequency structural components within the time–frequency images, thereby enhancing the model's representational capability.
(3) By jointly considering the high-dimensional space of images and the latent space, we construct a two-dimensional feature space describing normal samples. Then, one-class SVM is utilized to learn the boundary of the feature space for anomaly detection.

2. Radar Multipath Effects

Radar multipath effect refers to the phenomenon wherein a wave, during its propagation from the transmitter to the target, traverses through multiple propagation paths. This effect captures scenarios where both a primary direct wave and several secondary indirect waves coexist at the receiving point. The received signal exhibits amplitude variations due to interference arising from the relative phase alignments between the direct and indirect waves. Specifically, different

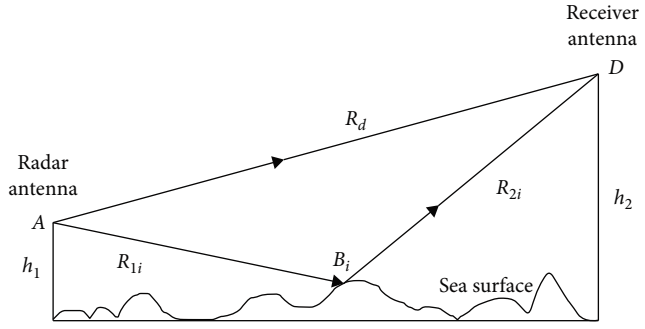

FIGURE 1: Schematic diagram illustrating multipath interference effects on sea surface signal propagation.

phase alignments lead to constructive or destructive summation of these waves at the receiver, thereby shaping the final observed amplitude variation of the signal.

Figure 1 presents a schematic diagram illustrating the multipath interference effects on radar signals propagating over the sea surface [16]. The direct propagation path $A \to D$ and the reflected paths $A \to B_i \to D$ contribute to the multipath interference, where i indicates the multiple reflected paths. In the figure, h_1 and h_2 represent the antenna heights of the radar and the receiver, respectively. Moreover, the path length of AD is denoted as Rd, while the path lengths of AB_i and B_iD are expressed as R_{1i} and R_{2i}, respectively. Under the multipath effect, signals arriving at the receiver through different propagation paths exhibit relative time delays due to the path length differences. Signals from various paths are superimposed at the receiver, and the resultant interference depends on the phases and amplitudes of each path signal. In addition, due to varying propagation paths, the signals undergo distinct levels of amplitude attenuation, phase shift, and Doppler frequency shift during propagation (especially when the reflecting surfaces or receiver are in motion). The composite signal at the receiving antenna can be expressed as follows:

$$S(t) = S_{\text{direct}}(t) \times H_{\text{direct}}(t) + \sum_{i=1}^{N} A_i \times S_{\text{direct}}(t - \tau_i) \times H_{\text{reflected},i}(t) \times e^{j(\phi_i + 2\pi f_d t)}, \tag{1}$$

where $S_{\text{direct}}(t)$ represents the direct path signal, N represents the total number of reflected paths. $H_{\text{direct}}(t)$ and $H_{\text{reflected},i}(t)$ are the attenuation and distortion models for the direct and i-th reflected signals, respectively. A_i represents the amplitude attenuation of the i-th reflected path, τ_i represents the time delay caused by the longer path length compared to the direct path, ϕ_i is the initial phase shift of the i-th reflected path, and f_d refers to the frequency shift due to the Doppler effect, which is related to the relative motion between reflecting objects and the receiver. Figure 2 presents the SPWVD time–frequency representations of four radar signal types, including linear frequency modulation (LFM), nonlinear frequency modulation (NLFM), binary phase shift keying (BPSK) and quadrature phase shift keying (QPSK), in both normal and multipath scenarios. Evident structural discrepancies exist between the time–frequency signatures of the normal and multipath signals, which could facilitate detection of the multipath interference.

3. Proposed Approach

3.1. Anomaly Detection Definition. Anomaly detection refers to the identification of abnormal samples that deviate significantly from the expected pattern of normal data distribution. In this paper, normal and abnormal samples are denoted by x and x', respectively. Let P_X and $P_{X'}$ represent the probability distributions of the normal and abnormal samples, respectively.

Our model is trained exclusively on the data set of normal samples according to P_X. During testing, the test set contains both normal (x) and abnormal (x') samples, where the distribution $P_{X'}$ of the abnormal samples differs from the normal distribution P_X.

The goal of our anomaly detection model is to assign each test sample an anomaly score that reflects its probability of belonging to the anomalous distribution $P_{X'}$. A higher score indicates a higher probability that the sample is abnormal (x'). By setting a threshold for the anomaly score, normal and abnormal samples can be effectively distinguished. The anomaly detection task can be formulated as finding a function $f : x \to s$, where x is the input sample and s is the anomaly score. The decision rule for classifying a sample as anomalous is:

$$\text{if } s > \tau, \text{ classify as abnormal } (x'). \tag{2}$$

The threshold τ depends on the desired tradeoff between true positive and false positive rates in detecting anomalies.

3.2. Model Architecture. Figure 3 presents the overall architecture of the proposed model, which comprises two modules: an autoencoder network with an attention mechanism and a feature extractor. In this structure, the input sample is first encoded and reconstructed by the autoencoder network, followed by the feature extractor learning the latent space of the samples.

The first subnetwork is an autoencoder network consisting of an encoder (*En*) and a decoder (*De*). The primary task of the autoencoder is to learn and reconstruct the input image. The primary task of the autoencoder is to learn and reconstruct the input image. Given an input image x, the encoder generates a latent vector z through downsampling, formulated as $z = En(x)$, where $z \in R^d$ $(d \ll w \times h \times c)$. The latent vector z is assumed to be the optimal low-dimensional representation of the input x. The encoder comprises convolutional layers, batch normalization, and leaky *ReLU* activation functions. To enhance the model's sensitivity to key high-energy line features and reduce attention on less significant background regions in the time–frequency images of Figure 2, we introduce the CBAM attention mechanism after each convolutional layer. The CBAM integrates both a channel attention submodule and a spatial attention submodule to strengthen the representational capability of convolutional

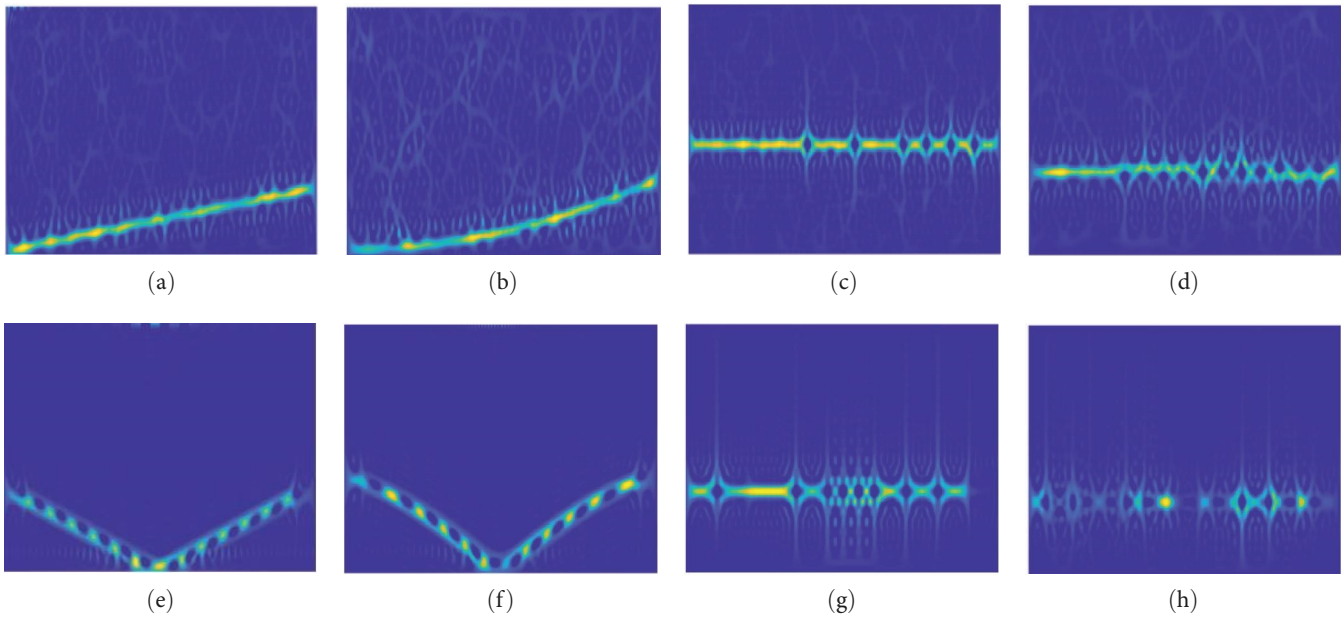

FIGURE 2: Two-dimensional time–frequency images extracted using SPWVD. Subfigures (a–d) represent the time–frequency images of normal LFM, NLFM, BPSK, and QPSK signals, respectively. Subfigures (e–h) represent the time–frequency images of the corresponding multipath LFM, NLFM, BPSK, and QPSK signals, respectively.

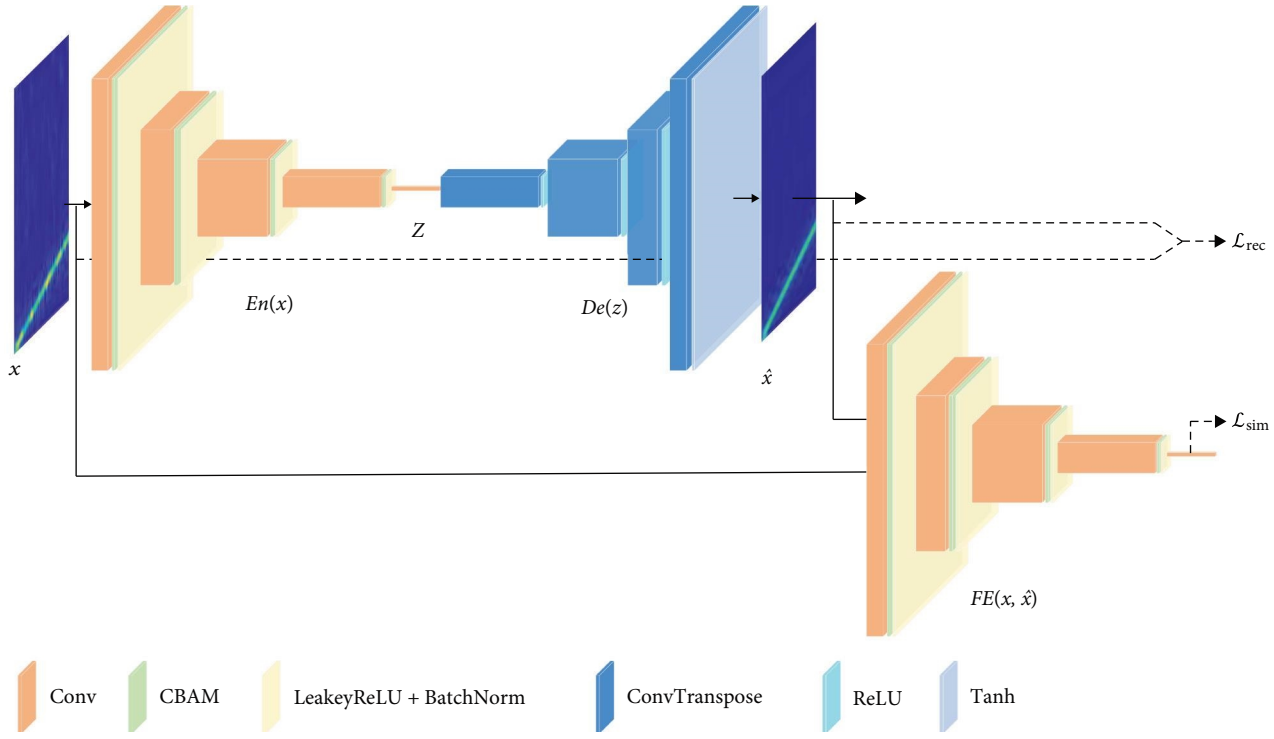

FIGURE 3: Schematic representation of the DADA model's architecture.

neural networks (CNNs). This allows the model to focus more on the relevant channels and spatial features.

3.2.1. Channel Attention Submodule. Given an input feature map $X \in R^{h \times w \times c}$, where h and w denote the height and width, respectively, and c represents the number of channels, this submodule aims to identify the more salient channels. The channel attention coefficients are computed as follows:

$$M_c = \sigma(\mathrm{MLP}(\mathrm{AvgPool}(X)) + \mathrm{MLP}(\mathrm{MaxPool}(X))). \tag{3}$$

Here, AvgPool and MaxPool refer to global average pooling and max pooling operations, respectively. MLP denotes multilayer perceptron, and σ is the sigmoid activation

function. This results in the final channel-wise enhanced feature map:

$$X' = M_c \otimes X, \tag{4}$$

where $\otimes$ denotes element-wise multiplication. M_c provides a scalar coefficient for each channel to multiply with all the spatial positions of the corresponding input channel.

3.2.2. Spatial Attention Submodule. This module aims to identify the more pertinent spatial regions. Taking the channel-wise feature map X' as input, the spatial attention coefficients are computed as follows:

$$M_s = \sigma(\mathrm{Conv}(\mathrm{AvgPool}(X')) + \mathrm{Conv}(\mathrm{MaxPool}(X'))), \tag{5}$$

where Conv represents the convolution operation. The resulting spatial attention enhanced feature map is as follows:

$$X'' = M_s \otimes X'. \tag{6}$$

By integrating channel and spatial attention, the CBAM module can effectively focus on the salient channels and spatial regions in the input feature. This allows the model to concentrate more precisely on task-relevant features, thus enhancing its representation capability.

Subsequently, through the upsampling process of the decoder (*De*), the input image x is reconstructed from the latent vector z, yielding the reconstructed image $\widehat{x} = De(z)$. The architecture of the decoder comprises deconvolutional layers, *ReLU* activations, and batch normalization, with a tanh layer applied to generate the final output.

The second subnetwork is the feature extractor (*FE*), which is inspired by the design of Siamese networks [17]. It shares the same architecture as *En* while having different parameterization. This network is designed to extract meaningful feature representations for the input image x and its reconstructed counterpart $\widehat{x}$. Through *FE*, we can obtain $v_x = FE(x)$ and $v_{\widehat{x}} = FE(\widehat{x})$, representing the latent features of the input and reconstructed images, respectively. These feature representations are used to evaluate the similarity between the input and reconstructed images. During testing, they can also be employed for anomaly detection.

3.3. Model Training. In this study, we train the model using only normal samples, aiming to enable the model to learn and reconstruct normal samples and capture their characteristics in the latent vector space. For the abnormal samples in the test set, as they are never trained on the model, the model struggles to achieve effective reconstruction. As a result, the feature extractor network computes the latent vectors v_x and $v_{\widehat{x}}$ for the input and reconstructed images, respectively, leading to a significant reduction in their similarity. To validate this process, we devise two objective functions to independently optimize each subnetwork to capture the key features of normal samples.

The first loss function is reconstruction loss. Similar to autoencoders, the reconstruction loss aims to minimize the discrepancy between the input sample x and its reconstructed counterpart $\widehat{x}$. This serves as a measure of the model's capability in learning and recovering the original normal sample characteristics. Formally, it is defined as follows:

$$L_{\mathrm{rec}} = E_{x \sim p\mathbf{X}} \parallel x - \widehat{x} \parallel_1. \tag{7}$$

By minimizing L_{rec}, the model is enabled to generate images closely resembling the normal samples.

The second loss function is the feature similarity loss. The inputs to this loss are from the original sample and reconstructed sample. During training with normal samples, the *FE* network extracts features from both the original samples x and the reconstructed samples $\widehat{x}$. Considering the reconstructed sample closely resembles the normal sample, the latent feature space, extracted by the *FE* network, is expected to exhibit minimal discrepancy. Therefore, we employ the feature similarity loss L_{sim} to optimize the model by minimizing the difference between the latent representations of the original input $v_x = FE(x)$ and the reconstructed image $v_{\widehat{x}} = FE(\widehat{x})$. L_{sim} is formally defined as follows:

$$L_{\mathrm{sim}} = E_{x \sim p\mathbf{X}} \parallel FE(x) - FE(\widehat{x}) \parallel_2^2. \tag{8}$$

3.4. Anomaly Detection with One-Class SVM. To enable effective anomaly detection, we incorporate the features extracted by the DADA model with a one-class SVM. For this purpose, two metrics are constructed to characterize normal sample patterns.

Reconstruction Similarity: This is defined by calculating the Euclidean distance between the original input X and its reconstructed counterpart $\widehat{X}$, reflecting the discrepancy between the input and reconstructed images. It is formulated as follows:

$$R(X) = \left\| X - \widehat{X} \right\|_2. \tag{9}$$

3.4.1. Latent Vector Similarity. This metric calculates the Euclidean distance between the latent vector V_X of the original input and $V_{\widehat{X}}$ of the reconstructed image, indicating the deviation between original and reconstructed inputs in the latent space. It is formulated as follows:

$$L(V) = \left\| V_X - V_{\widehat{X}} \right\|_2. \tag{10}$$

Based on the two metrics $R(X)$ and $L(V)$, a two-dimensional feature space can be constructed, where each training sample x_i is represented as a two-dimensional vector $[R(x_i), L(v_i)]$. This two-dimensional feature space serves as the input to the one-class SVM.

One-class SVM has been extensively utilized and demonstrated to be effective in anomaly detection tasks [18–20].

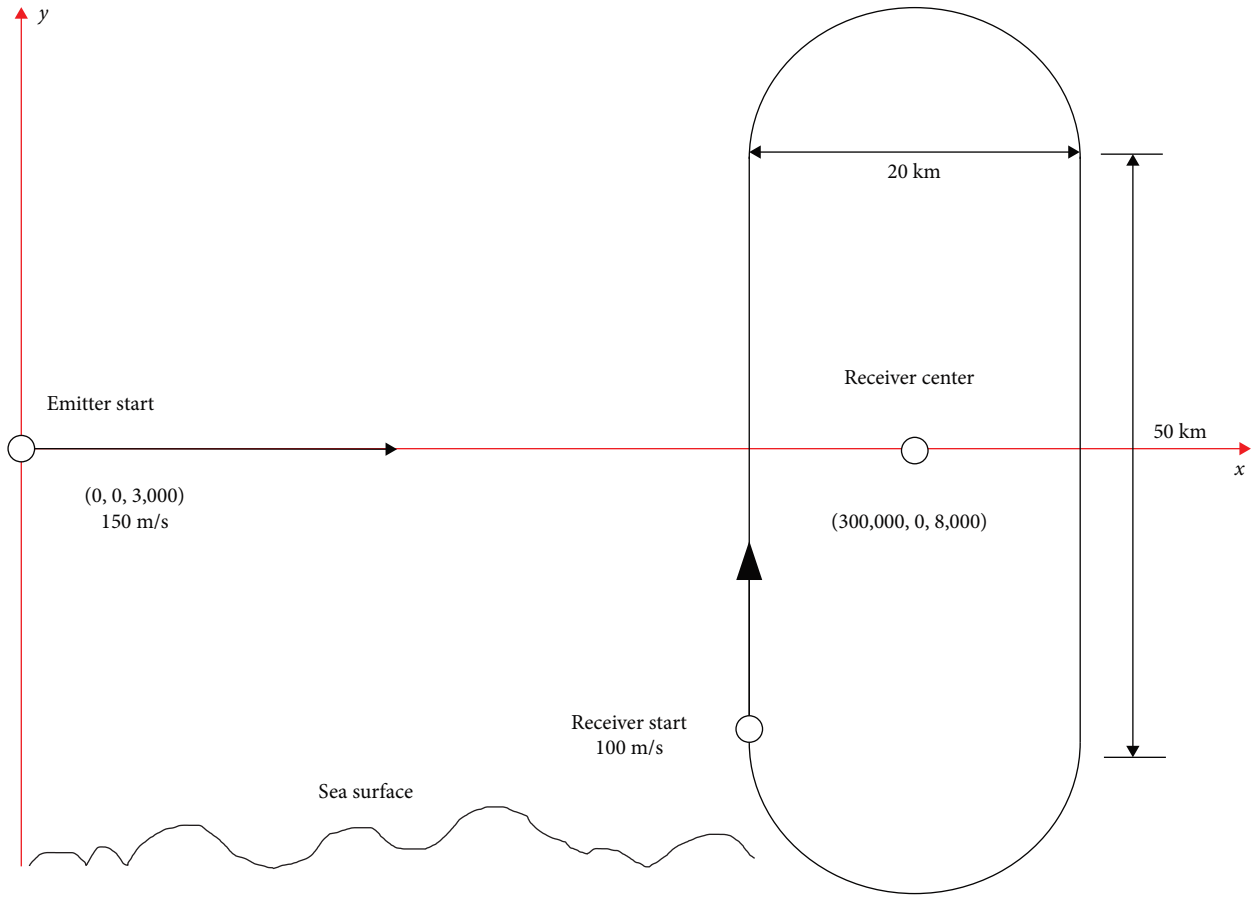

FIGURE 4: The schematic diagram of the simulation scenario [16].

Its fundamental concept involves identifying a hyperplane that maximizes the margin between the classes of normal and anomalous samples. Specifically, the feature space for normal samples is constructed to form the training dataset: $\{[R(x_1), L(v_1)], [R(x_2), L(v_2)], \ldots, [R(x_n), L(v_n)]\}$. Given this data set, one-class SVM seeks to address the following optimization problem:

$$\begin{aligned} &\min_{\mathbf{w},b,\xi} \frac{1}{2}|\mathbf{w}|^2 + \frac{1}{\delta n}\sum_{i=1}^{n}\xi_i - \rho \\ \text{Subject to}: \quad &\mathbf{w}\cdot\phi([R(x_i), L(v_i)]) \geq \rho - \xi_i \\ &\xi_i \geq 0 \end{aligned} \quad . \tag{11}$$

Here, $\mathbf{w}$ and b parameterize the separating hyperplane, $\phi(\cdot)$ transforms the data into a higher dimensional feature space, ξ_i signifies the training error, and δ governs the ratio of outliers.

Solving this optimization problem yields the decision function as follows:

$$f(x, v) = \text{sgn}(\mathbf{w}\cdot\phi([R(x), L(v)]) + b - \rho). \tag{12}$$

In this context, a test sample is categorized as normal if $f(x, v) > 0$; otherwise, it is considered an anomaly.

Following the detailed discussion above, the complete process of the DADA model is presented in Algorithm 1.

4. Experimental Results and Evaluation

4.1. Dataset: Details and Specifications. The dataset used in our experiments is derived from the "Radar Signal Simulation Platform under Complex Electromagnetic Environment" at the Southwest China Research Institute of Electronic Equipment. This platform employs a parabolic equation method to generate synthetic radar signal data. The parabolic equation technique serves as the foundation of radar signal processing by aligning and filtering the received echo signals with a reference signal identical to the transmitted one. This procedure yields a complex signal with a parabolic trajectory in the time domain. The simulated echo signals incorporate noise and Doppler effects to mimic real-world radar returns.

Figure 4 displays a representation of the simulated scenario incorporating multipath effects from sea surface reflections. These effects distort the received signal as it follows different propagation paths before arriving at the receiver. In the simulation, the receiver representing an aircraft at 8,000 m altitude follows a circular trajectory, while the transmitter at 3,000 m altitude moves along a linear path directing toward the circle's center. Both the transmitter and receiver are simulated using vertical polarization dipole antennas. The

Train Set: Normal radar signal dataset, transformed using SPWVD.
1: **for** a set number of training iterations
2: Minimize the reconstruction loss L_{rec} in Equation (7) to align $\hat{x}$ with x.
3: Minimize the feature similarity loss L_{sim} in Equation (8) to reduce the latent representation differences between x and $\hat{x}$.
4: **End for**
5: Construct a two-dimensional feature space from $R(X)$ and $L(V)$ using Equations (9) and (10).
6: Employ one-class SVM to learn the decision boundary for normal samples.

Algorithm 1: DADA.

transmitter power is set to 100 W with a gain of 20 dB and the receiver has a gain of 13 dB. Four signal types are generated in the simulation: LFM, NLFM, BPSK, and QPSK. The carrier frequency is uniformly fixed at 2,000 MHz for all signals. For LFM, the pulse width (PW) ranges from 5 to 15 μs and the bandwidth (BW) from 10 to 20 MHz. NLFM uses the same PW of 5–15 μs and BW of 10–20 MHz. For BPSK and QPSK, the number of subpulses ranges from 16 to 32, and the BW is from 2 to 5 MHz. To meet the requirements of the model, the training dataset contains 2,000 samples for each normal signal type. The test dataset comprises 200 samples per signal type, including both normal and multipath interference cases.

The radar signals are transformed into two-dimensional time–frequency images using the SPWVD technique to capture their dynamic spectral characteristics. SPWVD, an advanced time–frequency analysis method, jointly represents nonstationary signals in both time and frequency domains. Derived from the Wigner–Ville Distribution (WVD), SPWVD incorporates a smoothing kernel to mitigate the issues of cross-term interference and noise sensitivity associated with WVD. SPWVD achieves high-resolution signal representations, accurately capturing time-varying frequency content more than traditional techniques such as STFT and wavelet transform. This superior resolution is highly advantageous for analyzing and characterizing radar signals, where time–frequency features are vital for precise representation and detection. Figure 2 depicts the SPWVD-generated time–frequency images for both the normal and multipath interference signals across the four radar signal types.

4.2. Model Parameter Settings. In this work, we develop the model using the PyTorch deep learning framework. The experiments are implemented on a computer equipped with an RTX 3080 GPU and CUDA 11.7, running the Windows 10 operating system. The Adam optimizer is utilized to optimize the model with the following hyperparameter settings: learning rate $lr = 0.0002$, first momentum exponential decay rate $\beta_1 = 0.9$, second momentum exponential decay rate $\beta_2 = 0.999$, and numerical stability term $\varepsilon = 1e{-}8$.

4.3. Performance Analysis with Varying Multipath Interference Signals. In this study, we employ various evaluation metrics to assess the performance of the anomaly detection model. These metrics include:

(1) Precision (P): Precision measures the proportion of true positive (TP) instances among the instances classified as positive by the model, calculated as $P = \mathrm{TP}/(\mathrm{TP} + \mathrm{FP})$, where FP represents false positives.
(2) Recall (R): Recall quantifies the proportion of true positive instances correctly identified by the model out of all true positive instances, calculated as $R = \mathrm{TP}/(\mathrm{TP} + \mathrm{FN})$, where FN represents false negatives.
(3) F1-score (F1): The F1-score is the harmonic mean of precision and recall, providing a single metric that combines both aspects. It is calculated as $\mathrm{F1} = 2 \times (\mathrm{P} \times \mathrm{R})/(\mathrm{P} + \mathrm{R})$.

These evaluation metrics allow for a comprehensive assessment of the anomaly detection model's performance, ensuring its effectiveness and reliability across various scenarios.

We assess the performance of our proposed method by analyzing test sets containing varying numbers of multipath interference signals. Specifically, we conduct four experiments, each involving a test set with an incrementally increasing number of multipath signals. To validate the effectiveness of the DADA model, this study conducts a comprehensive comparison between traditional radar signal feature extraction algorithms and deep learning models. For traditional algorithms, features are extracted from the time, frequency, and time–frequency domains. In the time domain, complexity features (CC) of the signals are extracted, including box dimension, information dimension, multiscale entropy, and sparsity. These features can effectively characterize the temporal dynamics of the signals [2–4]. In the frequency domain, key features based on spectral correlation (SC) are extracted, including the cyclic frequency peaks and core statistical parameters of the power spectral density (PSD), such as total power in the bandwidth, average power, variance of power, skewness, and kurtosis of the power distribution [21]. These frequency domain features aim to fully capture and describe the energy distribution and intrinsic nonstationarity of radar signals in the frequency domain. In the time–frequency domain, the wavelet ridge frequency cascade features (WRFCCF) of signals based on wavelet transform are extracted to depict statistical characteristics on the time–frequency plane by capturing instantaneous frequency information [22]. One-class SVM is utilized on the above extracted features for anomaly detection. For deep learning models, mainstream algorithms including AnoGAN [11], EGBAD [12], and GANomaly [13] are selected for comparison.

4.3.1. Experiment 1: Test Set with Single Multipath Signal. In this experiment, we evaluate the performance of our

Table 1: Performance metrics for the four methods (test set with single multipath signal).

Method	LFM (L)			NLFM (N)			BPSK (B)			QPSK (Q)		
	P	R	F1	P	R	F1	P	R	F1	P	R	F1
CCF	0.709	1.000	0.829	0.687	1.000	0.814	0.665	0.995	0.797	0.689	1.000	0.816
SC	0.657	1.000	0.793	0.678	1.000	0.808	0.586	1.000	0.739	0.664	1.000	0.798
WRFCCF	0.707	0.990	0.825	0.697	0.990	0.818	0.670	0.935	0.460	0.604	0.980	0.748
AnoGAN	0.673	0.970	0.795	0.803	0.960	0.874	0.498	0.995	0.664	0.593	0.870	0.705
EGBAD	0.668	0.995	0.799	0.921	0.995	0.956	0.505	0.990	0.669	0.619	0.975	0.757
GANomaly	0.872	1.000	0.931	0.854	0.899	0.876	0.576	0.953	0.719	0.898	0.605	0.723
DADA	1.000	0.980	0.990	1.000	0.960	0.979	0.731	0.925	0.817	0.866	0.905	0.885

Table 2: Performance metrics for the seven methods (test set with two multipath signals).

Method	LFM NLFM (LN)			LFM BPSK (LB)			LFM QPSK (LQ)		
	P	R	F1	P	R	F1	P	R	F1
CCF	0.639	1.000	0.779	0.671	0.997	0.802	0.667	1.000	0.800
SC	0.659	1.000	0.794	0.591	1.000	0.743	0.660	1.000	0.795
WRFCCF	0.675	0.950	0.789	0.610	0.700	0.651	0.621	0.927	0.744
AnoGAN	0.755	0.902	0.822	0.520	0.942	0.670	0.528	0.992	0.689
EGBAD	0.673	0.965	0.793	0.503	0.995	0.668	0.540	0.995	0.700
GANomaly	0.731	1.000	0.844	0.541	0.553	0.547	0.576	0.657	0.614
DADA	0.910	0.962	0.936	0.711	0.990	0.828	0.911	0.848	0.878

Table 3: Performance metrics for the seven methods (test set with two multipath signals).

Method	NLFM BPSK (NB)			NLFM QPSK (NQ)			BPSK QPSK (BQ)		
	P	R	F1	P	R	F1	P	R	F1
CCF	0.680	1.000	0.809	0.672	1.000	0.804	0.698	1.000	0.822
SC	0.586	1.000	0.739	0.672	1.000	0.804	0.592	1.000	0.744
WRFCCF	0.672	0.907	0.772	0.637	0.952	0.763	0.663	0.910	0.767
AnoGAN	0.507	0.990	0.671	0.518	0.995	0.681	0.542	0.985	0.699
EGBAD	0.558	0.987	0.712	0.579	0.990	0.731	0.591	0.985	0.739
GANomaly	0.684	0.632	0.655	0.657	0.953	0.777	0.980	0.514	0.674
DADA	0.745	0.992	0.851	0.905	0.937	0.921	0.800	0.910	0.851

proposed method on a test set containing a multipath interference signal to assess its ability to detect and handle a single interference source. The results are shown in Table 1.

4.3.2. Experiment 2: Test Set with Two Multipath Signals. In the second experiment, we increase the number of multipath interference signals in the test set to two to evaluate the robustness of our method when dealing with multiple sources of interference. The experimental results are shown in Tables 2 and 3.

4.3.3. Experiment 3: Test Set with Three Multipath Signals. The third experiment expands the test set to three multipath interference signals and evaluates the performance of our method in more complex scenarios with higher interference levels. The experimental results are shown in Table 4.

4.3.4. Experiment 4: Test Set with Four Multipath Signals. Finally, the fourth experiment evaluates our proposed method on a test set containing all four multipath interference signals, aiming to demonstrate its effectiveness in handling the most challenging cases under high interference levels. The results are shown in Table 5.

As shown in Tables 1–5, our proposed method achieves superior F1-scores compared to other methods across all datasets. It is observed that the model finds it relatively easy to process test sets containing only a single multipath interference signal, achieving the best performance on LFM and NLFM with F1-scores of 0.990 and 0.979, respectively. In comparison, the performance on BPSK and QPSK declines slightly, indicating greater challenges in detecting anomalies for these signal types.

As more multipath signal types are included in the test set, the overall performance of all methods decreases, especially when BPSK signals are present. This further highlights the difficulty that BPSK signals pose for anomaly detection. Although the CCF and SC methods achieve 100% recall,

Table 4: Performance metrics for the seven methods (test set with three multipath signals).

Method	LFM NLFM BPSK (LNB)			LFM NLFM QPSK (LNQ)			LFM BPSK QPSK (LBQ)			NLFM BPSK QPSK (NBQ)		
	P	R	F1	P	R	F1	P	R	F1	P	R	F1
CCF	0.660	1.000	0.795	0.656	1.000	0.792	0.673	1.000	0.804	0.677	1.000	0.807
SC	0.591	1.000	0.743	0.664	1.000	0.798	0.583	1.000	0.736	0.584	1.000	0.738
WRFCCF	0.660	0.906	0.764	0.637	0.926	0.755	0.651	0.925	0.764	0.663	0.930	0.774
AnoGAN	0.540	0.950	0.688	0.557	0.918	0.693	0.522	0.985	0.682	0.536	0.963	0.689
EGBAD	0.545	0.985	0.701	0.516	0.986	0.677	0.562	0.986	0.716	0.513	0.995	0.677
GANomaly	0.762	0.622	0.685	0.948	0.740	0.831	0.545	0.846	0.663	0.852	0.600	0.704
DADA	0.759	0.951	0.845	0.872	0.965	0.916	0.736	0.991	0.845	0.740	0.978	0.843

Table 5: Performance metrics for the seven methods (test set with four multipath signals).

Method	LFM NLFM BPSK QPSK (LNBQ)		
	P	R	F1
CCF	0.668	1.000	0.801
SC	0.672	1.000	0.804
WRFCCF	0.644	0.907	0.753
AnoGAN	0.534	0.938	0.681
EGBAD	0.515	0.998	0.680
GANomaly	0.649	0.550	0.595
DADA	0.787	0.902	0.841

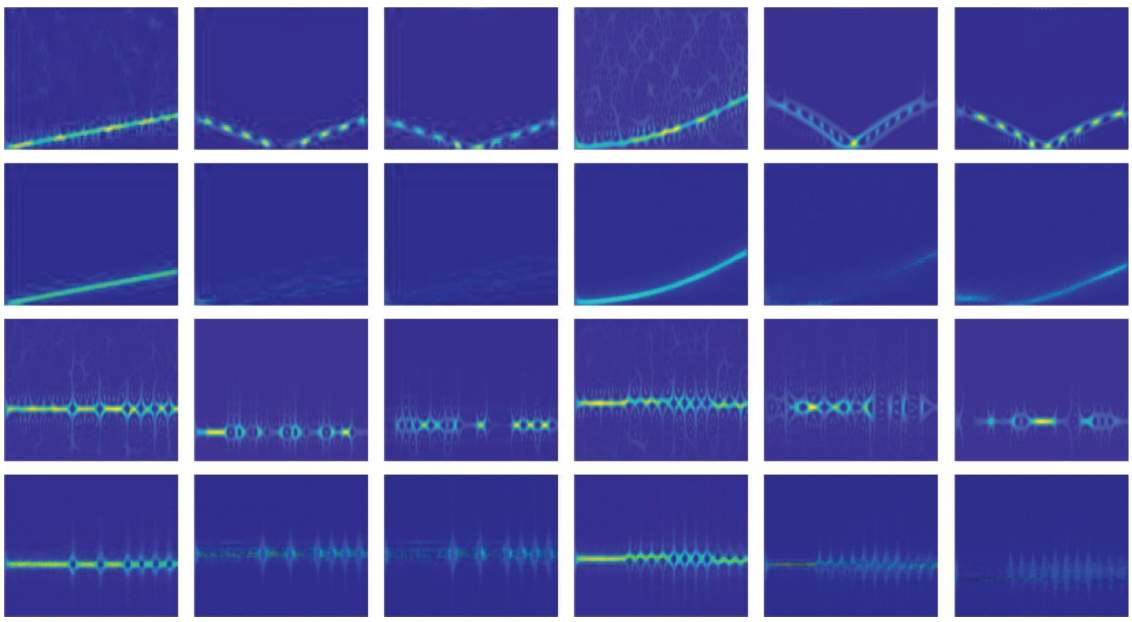

Figure 5: Comparison of input images and generated images using the autoencoder. The figure consists of four rows of images. Rows 1 and 3 show the input images, respectively, while Rows 2 and 4 display the corresponding generated images.

their F1-scores are lower. The performance degradation with more signal types is more pronounced for deep learning models such as AnoGAN, EGBAD, and GANomaly, especially on the test set with all four multipath signals. Our method consistently shows better overall performance and is more robust in complex environments.

Figures 5 and 6 illustrate the model's reconstruction on the test set signals. Figure 5 shows the reconstructed images when the test set contains single multipath signal. For each signal type, the first image represents the normal signal, and the other two are multipath interference signals. It is observed that the model can effectively reconstruct normal

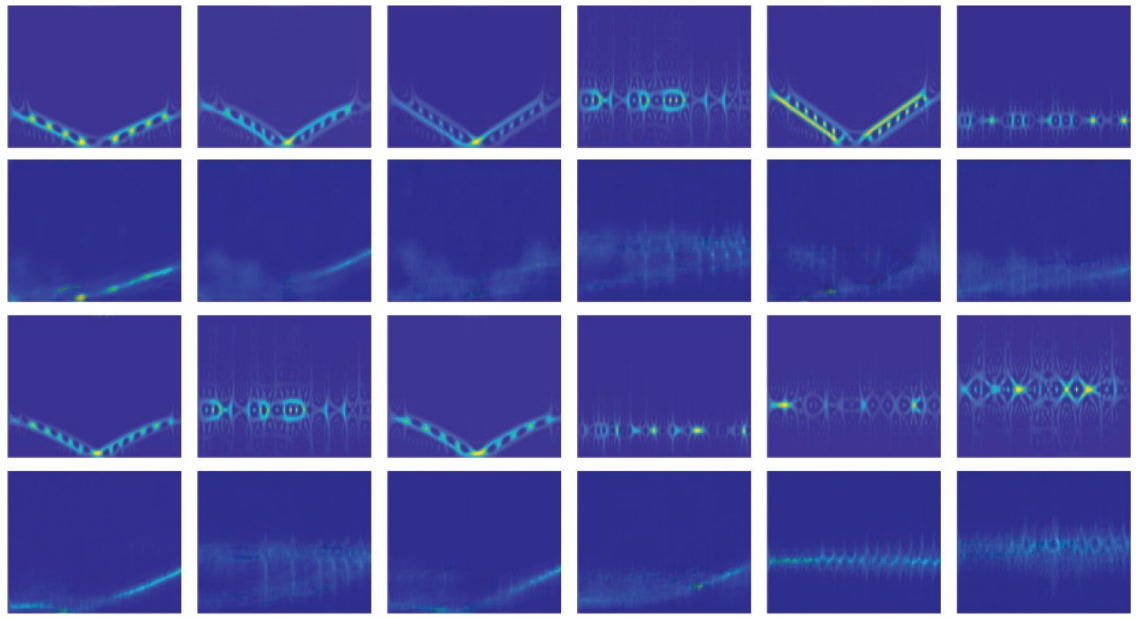

Figure 6: Comparison of input images and generated images using the autoencoder for another set of data. The organization of this figure is similar to Figure 5. Rows 1 and 3 show the input images, respectively, while Rows 2 and 4 display the corresponding generated images.

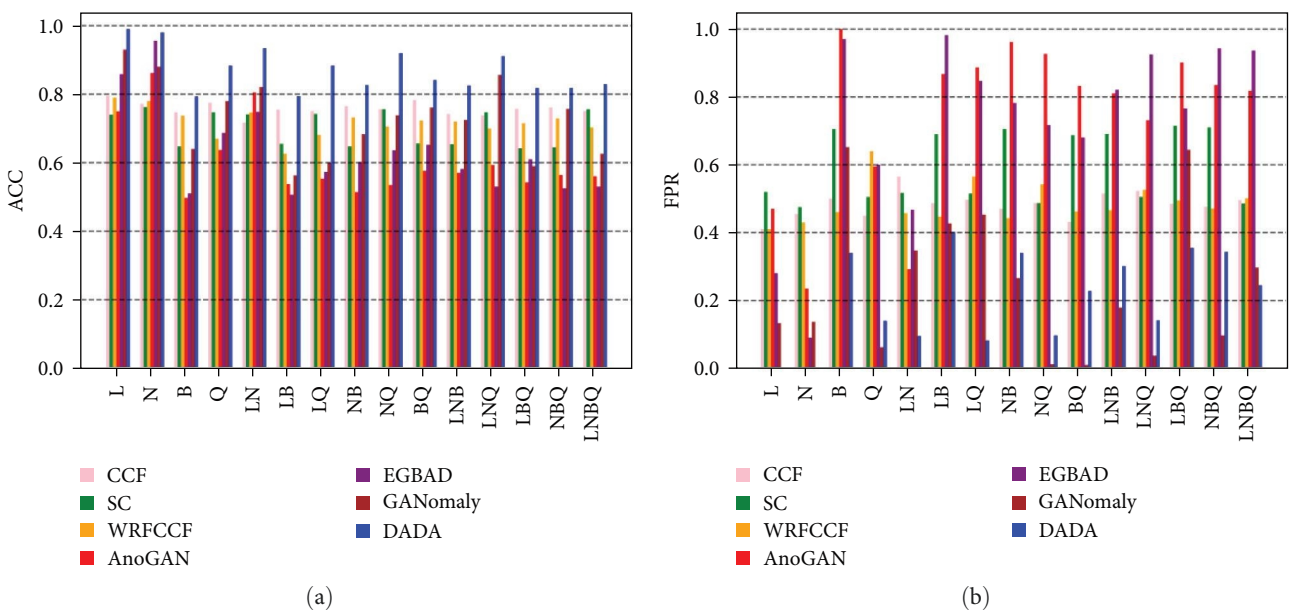

Figure 7: Comparative evaluation of different methods based on ACC and FPR on all datasets: (a) ACC comparison and (b) FPR comparison.

signals but struggles with anomalous multipath signals, since it only learns normal signal characteristics. Figure 6 displays the reconstructions when two multipath signal types are present in the test set. As the model performs well on normal signals, all images here contain multipath signals. Compared to Figure 5, slight distortions emerge when reconstructing signals in Figure 6, e.g., LFM features appearing in BPSK multipath signals, possibly due to the inclusion of information from both normal signal types during reconstruction. Nevertheless, the model remains unable to properly reconstruct multipath signals, which facilitates anomaly detection. Experiments 3 and 4 show similar reconstruction performance with more multipath signal types, further demonstrating the correlation between the model's anomaly detection capability and the number and types of multipath signals in the test set. In summary, the model can reconstruct normal signals well but fails to effectively reconstruct multipath signals. Also, its reconstruction capability declines with more signal types in the test set, yet anomalous signals can still be successfully identified. This validates that the model can effectively detect anomalies by learning the characteristics of normal signals.

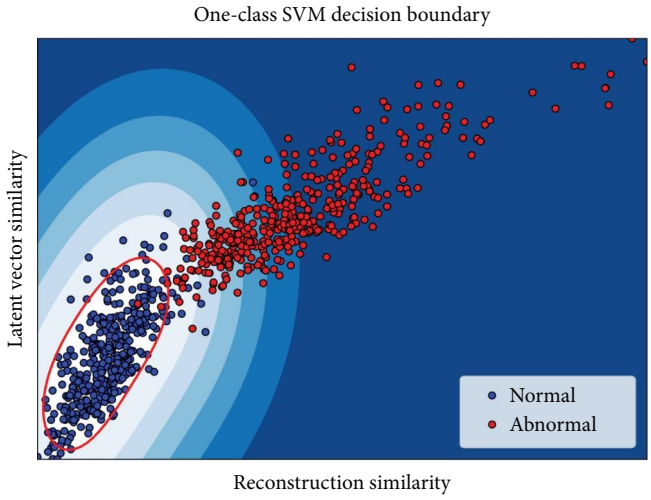

FIGURE 8: One-class SVM decision boundary delineating normal and abnormal samples in feature space.

To more comprehensively evaluate the model performance, Figures 7(a) and 7(b) present the accuracy (ACC) and false positive rate (FPR) of different methods on all datasets, respectively. The ACC reflects the model's capability in correctly recognizing all instances. A higher ACC signifies that the model can effectively distinguish between positive and negative samples, demonstrating its overall classification performance. The FPR refers to the proportion of negative samples incorrectly classified as positive, which is especially critical for anomaly detection tasks since it directly correlates to the number of false alarms. A lower FPR denotes that the model excels at avoiding mislabeling normal samples as anomalies. Our method attained higher ACC and lower FPR on most datasets, with FPR being 0 on LFM and NLFM datasets. These results further validate the efficacy of our proposed method.

Figure 8 illustrates the decision boundary delineated by the one-class SVM for normal and abnormal samples within the test data of the LN dataset. The model effectively encapsulates the majority of the normal data points within the decision boundary, which is shown as an elliptical contour. Notably, the normal samples are predominantly inside the ellipse, while the abnormal samples are largely outside the ellipse, indicating a clear separation of the two classes by the model.

Overall, these results demonstrate that the proposed method offers improved anomaly detection performance, surpassing previous advanced techniques.

5. Conclusion

To address the issue of multipath interference detection in radar signals, we have proposed a semisupervised anomaly detection approach called DADA in this study. The method is trained exclusively on normal signals. By extending the autoencoder architecture and incorporating a feature extractor network, it can capture the latent feature space of the samples. To better extract the time–frequency characteristics of radar signals, a CBAM attention mechanism is introduced to enhance feature learning. The method jointly considers the high-dimensional image space and the low-dimensional feature space, constructs a two-dimensional feature space representing normal samples, and performs anomaly detection by learning the feature space boundary using one-class SVM. The effectiveness of the proposed approach is validated through extensive experiments on multiple datasets in each experimental group. Reconstruction analysis shows that DADA can effectively reconstruct normal signals, but fails for multipath signals. Results show that DADA consistently achieves higher accuracy and F1-scores compared to benchmarks, and exhibits greater robustness when more signal types are present in the test set. Our future work will evaluate the generalizability of the method on more datasets.

Data Availability

The data that support the findings of this study are available from the corresponding author upon reasonable request.

Conflicts of Interest

The authors declare there are no conflicts of interest.

Acknowledgments

This study is financially supported by the Science and Technology on Electronic Information Control Laboratory, Grant/Award Number: 6142105190312 and the National Natural Science Foundation of China, Grant/Award Number: 62201097.

References

[1] S. L. Wilson and B. D. Carlson, "Radar detection in multipath," *IEE Proceedings - Radar, Sonar and Navigation*, vol. 146, no. 1, pp. 45–54, 1999.

[2] L. Yibing and L. Jingchao, "The identification of communication signals based on fractal box dimension and index entropy," *Journal of Convergence Information Technology*, vol. 6, no. 11, pp. 201–208, 2011.

[3] G. Zhang, L. Hu, and J. Weidong, "Intra-pulse feature analysis of radar emitter signals," *Journal of Infrared and Millimeter Waves*, vol. 23, no. 6, pp. 477–480, 2004.

[4] Q. Fu, C. Li, F. Cai, W. Wang, and S. Xiao, "Emitter signal sorting based on fractal dimensions of pulse envelope's front edge," in *2016 International Conference on Military Communications and Information Systems (ICMCIS)*, pp. 1–5, IEEE, Brussels, Belgium, May 2016.

[5] J. Lunden and V. Koivunen, "Automatic radar waveform recognition," *IEEE Journal of Selected Topics in Signal Processing*, vol. 1, no. 1, pp. 124–136, 2007.

[6] G. Lopez-Risueno, J. Grajal, and A. Sanz-Osorio, "Digital channelized receiver based on time–frequency analysis for signal interception," *IEEE Transactions on Aerospace and Electronic Systems*, vol. 41, no. 3, pp. 879–898, 2005.

[7] T. Ravi Kishore and K. D. Rao, "Automatic intrapulse modulation classification of advanced LPI radar waveforms," *IEEE Transactions on Aerospace and Electronic Systems*, vol. 53, no. 2, pp. 901–914, 2017.

[8] Y. Liu, P. Xiao, H. Wu, and W. Xiao, "LPI radar signal detection based on radial integration of Choi-Williams time-

frequency image," *Journal of Systems Engineering and Electronics*, vol. 26, no. 5, pp. 973–981, 2015.

[9] Z. Pan, S. Wang, and Y. Li, "Residual attention-aided U-Net GAN and multi-instance multilabel classifier for automatic waveform recognition of overlapping LPI radar signals," *IEEE Transactions on Aerospace and Electronic Systems*, vol. 58, no. 5, pp. 4377–4395, 2022.

[10] L. Liu and X. Li, "Unknown radar waveform recognition system via triplet convolution network and support vector machine," *Digital Signal Processing*, vol. 123, Article ID 103439, 2022.

[11] T. Schlegl, P. Seeböck, S. M. Waldstein, U. Schmidt-Erfurth, and G. Langs, "Unsupervised anomaly detection with generative adversarial networks to guide marker discovery," in *Information Processing in Medical Imaging*, M. Niethammer, M. Styner, and S. Aylward, et al., Eds., pp. 146–157, Springer International Publishing, Springer, Cham, 2017.

[12] H. Zenati, C. S. Foo, B. Lecouat, G. Manek, and V. R. Chandrasekhar, "Efficient GAN-based anomaly detection," 2018.

[13] S. Akcay, A. Atapour-Abarghouei, and T. P. Breckon, "GANomaly: semi-supervised anomaly detection via adversarial training," in *Computer Vision—ACCV 2018*, C. V. Jawahar, H. Li, G. Mori, and K. Schindler, Eds., pp. 622–637, Springer International Publishing, Springer, Cham, 2019.

[14] S. Akçay, A. Atapour-Abarghouei, and T. P. Breckon, "Skip-GANomaly: skip connected and adversarially trained encoder–decoder anomaly detection," in *2019 International Joint Conference on Neural Networks (IJCNN)*, pp. 1–8, IEEE, Budapest, Hungary, July 2019.

[15] M. Sabokrou, M. Khalooei, M. Fathy, and E. Adeli, "Adversarially learned one-class classifier for novelty detection," in *Proceedings of the IEEE Conference on Computer Vision and Pattern Recognition*, pp. 3379–3388, IEEE, 2018.

[16] K. Yan, W. Jin, Y. Huang, P. Song, and Z. Li, "Deep adaptive temporal network (DAT-Net): an effective deep learning model for parameter estimation of radar multipath interference signals," *EURASIP Journal on Advances in Signal Processing*, vol. 2023, no. 1, Article ID 94, 2023.

[17] G. Koch, R. Zemel, and R. Salakhutdinov, "Siamese neural networks for one-shot image recognition," in *Proceedings of the 32 nd International Conference on Machine Learning, Lille, France*, W&CP, JMLR, 2015.

[18] B. Schölkopf, J. C. Platt, J. Shawe-Taylor, A. J. Smola, and R. C. Williamson, "Estimating the support of a high-dimensional distribution," *Neural Computation*, vol. 13, no. 7, pp. 1443–1471, 2001.

[19] M. Amer, M. Goldstein, and S. Abdennadher, "Enhancing one-class support vector machines for unsupervised anomaly detection," in *ODD '13: Proceedings of the ACM SIGKDD Workshop on Outlier Detection and Description*, pp. 8–15, Association for Computing Machinery, New York, NY, USA, August 2013.

[20] S. M. Erfani, S. Rajasegarar, S. Karunasekera, and C. Leckie, "High-dimensional and large-scale anomaly detection using a linear one-class SVM with deep learning," *Pattern Recognition*, vol. 58, pp. 121–134, 2016.

[21] A. Napolitano, *Generalizations of Cyclostationary Signal Processing: Spectral Analysis and Applications*, John Wiley & Sons, 2012.

[22] Z. B. Yu, W. D. Jin, and C. X. Chen, "Radar emitter signal recognition based on WRFCCF," *Journal of Southwest Jiaotong University*, vol. 45, no. 2, pp. 290–295, 2010.